Computational Geosciences (2023) 27:317–335
https://doi.org/10.1007/s10596-023-10198-2

ORIGINAL PAPER

Three-dimensional numerical simulation of hydraulically driven cohesive fracture propagation in deformable reservoir rock using enriched EFG method

Mohammad Ali Iranmanesh[1] · Ali Pak[2]

Received: 14 January 2022 / Accepted: 13 February 2023 / Published online: 15 March 2023

Abstract
In this paper, a fully coupled 3D. numerical simulation of hydraulic fracture propagation in saturated deformable porous media is presented in the context of the extrinsically enriched element free Galerkin (EFG) method. By exploiting the partition of unity property of moving least square shape functions, weak and strong discontinuities are simulated using the Ridge and the Heaviside enrichment functions, respectively. The cohesive crack model is used to describe the nonlinear fracture processes developing in the area in front of the crack tip where the energy dissipation takes place. The fracturing fluid flow within the fracture is modeled using Darcy's law and the fracture permeability is considered to follow the cubic law. The developed fully coupled numerical framework can simulate the fluid leak-off phenomenon and formation of the fluid-lag zone. For verification of the developed computational algorithm, a problem with an analytical solution was simulated and a good agreement was seen between numerical and analytical results. The numerical simulations and the parametric studies results show that the proposed numerical framework can successfully simulate various aspects of the complicated process of the hydraulic fracturing treatment.

Keywords Enriched element free Galerkin · Extrinsic PUM enrichment · Hydraulic fracturing · Cohesive crack model · Fully coupled numerical analysis

1 Introduction

The process of pumping a viscous fluid into the underground formations at high injection rates, to hydraulically propagate an induced fracture, is called Hydraulic Fracturing. This technique has become very attractive, because of its wide range of practical applications in many engineering disciplines. For instance, in the petroleum industry, hydraulic fracturing is the most commonly used stimulation technique to enhance oil recovery from damaged or unconventional reservoirs [1]. Other applications of this technology include radioactive waste disposal, measuring the in-situ stress field in deep rock layers, improving the performance of in situ remediation of contaminated soils [2], geothermal energy extraction [3], etc. Various applications of this technology have motivated industry to investigate the mechanisms associated with the initiation and propagation of hydraulically driven fractures in different porous media such as rocks.

Studying various aspects of hydraulic fracturing started with an analytical investigation of injecting an incompressible fluid into an elastic impermeable medium under simple plane strain and axisymmetric conditions. The first analytical solutions of hydraulic fracturing were the works conducted by Khristianovic and Zheltov [4] and Geertsma and de Klerk [5] (named Khristianovic-Geertsma-de Klerk or KGD) as well as Perkins and Kern [6] and Nordgren [7] which lead to the well-known Perkins-Kern-Nordgren (PKN) model. Geertsma and de Klerk [5] proposed an analytical solution for the calculation of the width and extent of hydraulically induced fractures (KGD model). In their approach, a viscous Newtonian fluid is pumped at a constant flow rate to hydraulically propagate a vertical fracture in an infinite saturated porous medium, assuming incompressible fluid and impermeable porous medium.

Hydraulic fracturing is a complicated multi-physics problem, hence analytical solutions, due to their simplifying

✉ Mohammad Ali Iranmanesh
iranmanesh@kntu.ac.ir

[1] Department of Civil Engineering, K. N. Toosi University of Technology, Tehran, Iran

[2] Department of Civil Engineering, Sharif University of Technology, Tehran, Iran

assumptions, are not able to consider all essential aspects, and hence, numerical simulation is required for a thorough analysis of hydraulic fracturing. A comprehensive simulation of this process requires a multitude of phenomena, including (I) the fluid flow within the fracture, (II) the fluid flow through the host medium, (III) the fluid leak-off from the fracture into the surrounding porous rock, (IV) the deformation of the surrounding medium due to the hydraulic loading and (V) the crack propagation. A strong hydro-mechanical coupling exists between the governing partial differential equations of the system, including the equations of solid skeleton deformation, fluid flow in the porous medium and fluid flow through the fracture. Limitations associated with the nature of analytical solutions compelled the research stream to turn into developing numerical algorithms, primarily based on the finite element method (FEM) and, more recently using extended finite element method (XFEM). This study aims to prepare a robust and efficient numerical tool for the analysis and design of the hydraulic fracturing process, which can be used for academic as well as industrial purposes.

So far, several numerical approaches have been used to simulate the processes of initiation and propagation of fluid-driven fractures in porous media. In some of them, the host medium is considered as a non-porous material e.g. Settari [8], Adachi et al. [9], Yamamoto et al. [10] and Yamamoto et al. [11], while many others treated the surrounding medium as permeable porous material. For example, by combining the finite element method with the finite difference method, Boone and Ingraffea [12] simulated the process of hydraulic fracturing in poroelastic materials. Desroches and Thiercelin [13] developed a numerical algorithm to simulate the propagation of a planar crack due to injecting a Newtonian fluid in a homogeneous elastic media. Pak [14] investigated the process of propagation of hydraulically driven fractures, incorporating thermal effect by using a full coupled THM numerical analysis. By exploiting the advantages of the cohesive crack model and the using adaptive finite element method, Simoni and Secchi [15] and Secchi et al. [16] simulated the hydraulic fracture process. Using the extended finite element method, Rethore et al. [17, 18] simulated the fluid flow inside the fracture. The use of zero-thickness interface elements in the finite element method for the simulation of hydraulic fracturing was presented by Lobao et al. [19]. Khoei et al. [20] and Barani et al. [21] simulated the fracture propagation in saturated and partially saturated porous media by using the adaptive finite element method and cohesive interface elements. Mohammadnejad and Khoei [22, 23] conducted an extended finite element modeling and simulated hydraulic fracturing by using a cohesive crack model in saturated and unsaturated porous media. The three-phase XFEM modeling of cohesive hydraulic fracture is presented by Salimzadeh and Khalili [24]. Hydraulic fracture propagation in impermeable cohesive porous media with frictional natural faults is simulated by Khoei et al. [25]. Modeling interaction between hydraulically driven fractures and natural faults is conducted by Khoei et al. [26] using the extended finite element method. The propagation of hydraulic fracturing in naturally layered media is simulated by Vahab et al. [27] using the extended finite element method. Vahab and Khalili [28] exploited XFEM for simulating fluid-lag phenomenon in hydraulic fracturing treatment. They also presented a staggered algorithm for hydraulic fracture simulation [29]. Mortazavi et al. [30] simulated cold and hot water injection into naturally fractured porous media using the extended–FEM and an equivalent continuum model. Many other types of research are available in the literature [31, 32].

This paper presents the simulation of hydraulically driven fractures in porous deformable rocks in the context of the enriched element-free Galerkin method, which is an extension of the well-known EFG[1] mesh-less method. It has been proven that the mesh-less methods are powerful numerical tools and proper alternatives to FEM to overcome the difficulties associated with the conventional methods for simulating discontinuities. Because of using shape functions with higher order of continuity for interpolating the unknown variables, stress fields are more accurate in mesh-less methods compared to FEM. Moreover, it is proven that for simulating problems with moving boundaries and discontinuities, meshless methods are powerful numerical tools [33–35]. More information about the mesh-less methods, their applications and programming techniques are available in [36, 37]. Applications of the mesh-less methods, especially the EFG method, for the simulation of coupled hydro-mechanical problems are illustrated by Modaressi and Aubert [38], Oliaei et al. [39], Khoshghalb and Khalili [34, 40], Soares [41], Tootoonchi et al. [42], Ghaffaripour et al. [43], Samimi and Pak [44–46] and Iranmanesh et al. [35].

Generally in mesh-less methods, strong discontinuities (such as cracks and impermeable discontinuities, where the field variables are discontinuous) can be simulated using weight function modification methods (visibility, diffraction and transparency) [47, 48], intrinsic basis functions modification [49] and extrinsic PUM[2] enrichment [33, 50, 51]. Moreover, to introduce weak discontinuities inside the domain (like the interface of two materials, where the field variables are continuous while their first derivatives are discontinuous) in mesh-less methods, employing the constrained mesh-less methods (Lagrange multipliers and penalty) [36, 52] and extrinsic enrichment [33, 50, 53] have been recommended in the literature. Iranmanesh and Pak utilized an extrinsic enrichment strategy in the context of element free Galerkin method to simulate the thermo-

[1] Element Free Galerkin
[2] Partition of Unity Method

hydro-mechanical processes in saturated porous media containing weak and strong discontinuities [54]. For simulating Hydraulic fracturing by using element-free Galerkin method, Oliaei et al. [55] presented the simulation of hydraulic fracturing in saturated porous media using two criteria for tensile and shear failures. Samimi and Pak [56] exploited the diffraction approach for modeling the hydraulically-driven fractures in element free Galerkin method. They used linear elastic fracture mechanics concepts and stress intensity factors as the propagation criterion.

The main objective of this paper is to establish a fully coupled enriched EFG approach to simulate the propagation of hydraulically driven fractures in porous deformable rocks by taking advantage of cohesive fracture mechanics. To achieve this goal, the generalized Biot theory [57] is utilized in conjunction with the cohesive crack model for describing the coupling among geomechanical behavior, fluid mass transfer, and fracture propagation aspects in hydraulic fracture treatments. The cohesive crack model is used to describe the nonlinear fracture processes developing in the area in front of the crack tip where the energy dissipation takes place [58]. The host rock matrix is assumed as a deformable porous media and the fluid leak-off from the fracture medium into the host rock matrix is considered. In addition, the size of the region between the crack tip and the fracturing fluid front along the fracture, which is called "the fluid lag zone", and the corresponding fluid pressure gradient, can be obtained through the fully coupled hydro-mechanical analysis. The resulting fully coupled and nonlinear algebraic system of equations is solved using the iterative Newton-Raphson algorithm.

The paper is organized as follows: In the next section, first, partial differential equations governing the general process of hydraulic fracturing are described, and their numerical discretization is presented in the context of the enriched element-free Galerkin method. In section 3, the basics of the enriched element-free Galerkin (XEFG) method are presented. In section 4, the cohesive crack model is briefly introduced. Section 5 is devoted to the numerical verification of the proposed algorithm along with the parametric study on some parameters influencing the hydraulic fracturing process. Finally, concluding remarks are presented in section 6.

2 Formulation

2.1 Governing equations

As stated before, the complicated process of hydraulic fracturing is the result of interaction between various physical phenomena, including the deformation of the solid skeleton, fluid flow through the porous medium surrounding the fracture, fluid flow through the fracture, leak-off of the fracturing fluid into the host medium and finally crack propagation. Accordingly, considering solid phase displacement ($\mathbf{u}$) and pore fluid pressure (p_w) as the main unknown variables, the set of partial differential equations for fully coupled numerical simulation of hydraulic fracture propagation in saturated porous media is stated as follows [20, 23, 59]:

(1) The linear momentum balance equation for the whole mixture:

$$\boldsymbol{\sigma}_{ij,j} + \rho \mathbf{g}_i = 0 \tag{1}$$

(2) The continuity equation for the pore fluid flow through the host medium:

$$\left[\frac{\alpha - n}{K_s} + \frac{n}{K_w}\right]\frac{\partial p_w}{\partial t} + \alpha\, \dot{\mathbf{u}}_{i,i} + \frac{1}{\rho_w}\left[\rho_w n\, \dot{\mathbf{u}}_i^{ws}\right]_{,i} = 0 \tag{2}$$

(3) The continuity equation for the fluid flow within the fracture:

$$\frac{1}{K_w}\frac{\partial p_w}{\partial t} + \frac{1}{w}\frac{\partial w}{\partial t} + \frac{1}{\rho_w}\left[\rho_w \overline{\mathbf{v}}_{wi'}\right]_{,i'} = 0 \tag{3}$$

Where $\boldsymbol{\sigma}_{ij}$ denotes the total stress tensor, ρ is the average density of the mixture that is defined as $\rho = (1-n)\rho_s + n\rho_w$ and n is porosity that is defined as the ratio of the volume of voids to the total sample volume. ρ_s and ρ_w are the solid and pore fluid phase densities, respectively, $\mathbf{g}_i$ denotes the acceleration of gravity vector, w is the crack opening and α denotes Biot's parameter that is defined as $\alpha = 1 - K_T/K_S$. Parameters K_T, $K_S$and K_w are bulk moduli of the porous skeleton, solid grains and fluid phase, respectively. Furthermore, t indicates time and $\dot{\mathbf{u}}_i$ denotes the solid phase velocity vector. $\dot{\mathbf{u}}_i^{ws}$ is the relative velocity vector between the fluid phase and solid phase which is defined as follows:

$$n\dot{\mathbf{u}}_i^{ws} = \frac{\mathbf{k}_{ij}}{\mu_w}\left(-p_{w,j} + \rho_w \mathbf{g}_j\right) \tag{4}$$

Equation (4) denotes the linear momentum balance equation for the fluid phase which also known as Darcy's law. In this equation, $\mathbf{k}_{ij}$ is the tensor of intrinsic permeability, μ_w is the dynamic viscosity of pore fluid and $i, j = 1, 2, 3$. In Eq. (3), $\overline{\mathbf{v}}_{wi'}$ denotes the average velocity vector of the injected fluid that is defined through the momentum balance equation for a Newtonian fluid within the fracture (using the lubrication theory) as follows:

$$\overline{\mathbf{v}}_{wi'} = \frac{w^2}{12\mu_w}\left(-p_{w,i'} + \rho_w \mathbf{g}_{i'}\right) \tag{5}$$

Where $i^{'}=1, 3$ for defining the directions along the fracture length and height, respectively. According to the cubic law, the permeability of the crack with respect to the fracturing fluid is defined as $k_{wd}=w^2/(12f\mu_w)$, where f is a coefficient between 1.04 and 1.65 depending on the material properties, which takes into account the crack wall roughness effects on the fracturing fluid flow [60].

In order to incorporate the pore fluid pressure effects into the total stress tensor, it is necessary to exploit the modified Terzaghi's effective stress principle, which is stated as follows:

$$\boldsymbol{\sigma}_{ij}^{''} = \boldsymbol{\sigma}_{ij} + \alpha p_w \boldsymbol{\delta}_{ij} \tag{6}$$

Where $\boldsymbol{\sigma}_{ij}^{''}$ denotes the effective stress tensor and $\boldsymbol{\delta}_{ij}$ is the Kronecker delta. Also, the relationship between the effective stress tensor and the total strain tensor is stated through the following constitutive law:

$$\mathrm{d}\boldsymbol{\sigma}_{ij}^{''} = \mathbf{D}_{Tijkl}\,\mathrm{d}\boldsymbol{\varepsilon}_{kl} \tag{7}$$

Where $\mathbf{D}_{Tijkl}$ denotes the fourth-order tangential stiffness tensor of the material and $\mathrm{d}\boldsymbol{\varepsilon}_{kl}$ is the total strain increment tensor [61].

2.2 Initial and boundary conditions

The aforementioned set of governing equations must be solved numerically by considering proper initial and boundary conditions. Assuming the problem domain Ω as a porous media which is bounded by the external boundary Γ and internal discontinuity Γ_d, as shown in Fig. 1, the set of initial and boundary conditions are as follows:

- Initial conditions:

$$\mathbf{u}_i = \mathbf{u}_i^0, p_w = p_w^0 \text{at } t = 0 \textbf{ and } \text{on } \Omega \tag{8}$$

- Dirichlet boundary conditions:

$$\mathbf{u}_i = \overline{\mathbf{u}}_i \text{ on } \Gamma_u,\ p_w = \overline{p}_w \text{ on } \Gamma_{p_w} \tag{9}$$

- Neumann boundary conditions:

$$\begin{aligned} &\boldsymbol{\sigma}_{ij}\mathbf{n}_i = \overline{\mathbf{t}}_i \text{ on } \Gamma_\sigma \\ &\frac{\mathbf{k}_{ij}}{\mu_w}\left(-p_{w,j} + \rho_w \mathbf{g}_j\right)\mathbf{n}_i = \overline{\mathbf{q}}_w \text{ on } \Gamma_{q_w} \end{aligned} \tag{10}$$

- Internal boundary conditions along the discontinuity:

$$\begin{aligned} &\boldsymbol{\sigma}_{ij}\mathbf{n}_j = \mathbf{t}_{coh} - p_w \mathbf{n}_{\Gamma_d} \text{ on } \Gamma_d \\ &[\![\overline{v}_{wi}]\!] n_{\Gamma_d} = q_{L_w} \text{ on } \Gamma_d \end{aligned} \tag{11}$$

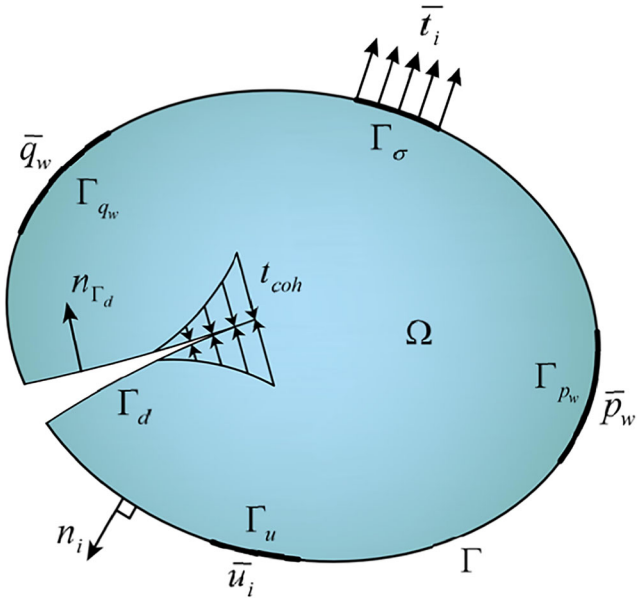

Fig. 1 Boundary conditions

In the above equations, $\mathbf{u}_i^0$ and p_w^0 are the initial values of the displacements and pore fluid pressure, respectively. The values of displacement ($\overline{\mathbf{u}}_i$) and pore fluid pressure ($\overline{p}_w$) are prescribed on different parts of the boundary Γ_u and Γ_{p_w} respectively. $\mathbf{n}_i$ is the outward unit vector normal to the external boundary. Moreover, $\overline{\mathbf{t}}_i$ and $\overline{\mathbf{q}}_w$ are defined as traction force and fluid flux vector on the boundaries Γ_σ and Γ_{qw}, respectively. $\mathbf{n}_{\Gamma_d}$ is the unit normal vector to the discontinuity line/surface Γ_d. As previously mentioned, t_{coh} denotes the cohesive tractions and q_{L_w} is the fluid leak-off flux from the fracture medium into the host porous rock. Note that the notation $[\![F]\!] = F^+ - F^-$ indicates the difference between the corresponding values of F at the two fracture faces.

2.3 Variational formulation

The constrained Galerkin weak form of the governing equations can be derived using the weighted residual method. Also, the penalty method must be used to enforce the essential boundary conditions presented in Eq. (9). The weak form of the linear momentum balance equation for the whole mixture can be obtained by integrating the product of this equation by admissible test function ω over the domain Ω as:

$$\int_\Omega \boldsymbol{\sigma}_{ij,j}\omega d\,\Omega + \int_\Omega \rho \mathbf{g}_i\,\omega d\,\Omega = 0 \tag{12}$$

Expanding the above equation by integration by parts, using Terzaghi's effective stress principle (Eq.(6)) and

applying the divergence theorem for discontinuous problems $\left(\int_{\Omega} div\mathbf{F}d\Omega = \int_{\Gamma} \mathbf{F}\cdot\mathbf{n}_{\Gamma}d\Gamma - \int_{\Gamma_d} [\![\mathbf{F}]\!]\cdot\mathbf{n}_{\Gamma_d}d\Gamma\right)$ lead to the following equation:

$$\int_{\Gamma_d} \boldsymbol{\sigma}_{ij}\,\omega.n_{\Gamma}d\Gamma - \int_{\Gamma_d} [\![\boldsymbol{\sigma}_{ij}\omega]\!] n_{\Gamma_d}d\Gamma - \int_{\Omega} \boldsymbol{\sigma}''_{ij}\omega_{,j}d\Omega + \int_{\Omega} \alpha p_w \boldsymbol{\delta}_{ij}\omega_{,j}d\Omega + \int_{\Omega} \rho\mathbf{g}_i\omega d\Omega = 0 \tag{13}$$

Substituting relations $\omega = \delta\mathbf{u}$ and $\omega_{,j} = \delta(L\mathbf{u})$ into Eq. (13) and introducing boundary conditions (Eqs. (9) to (11)) and also Eq. (7) into this equation results in the constrained Galerkin weak form of the equilibrium equation as follows:

$$\int_{\Omega} \delta(L\mathbf{u})^T \mathbf{D}_{T_{ijkl}} \boldsymbol{\varepsilon}_{kl}d\Omega - \int \delta(L\mathbf{u})^T \alpha p_w\, \boldsymbol{\delta}_{ij}d\Omega - \int_{\Gamma_\sigma} \delta\mathbf{u}^T\bar{\mathbf{t}}_i d\Gamma - \int_{\Omega} \delta\mathbf{u}^T \rho\mathbf{g}_i d\Omega + \delta\mathbf{u}^T\alpha_{p_u}\left(\mathbf{u}-\bar{\mathbf{u}}\right)d\Gamma + \int_{\Gamma_\sigma} [\![\delta\mathbf{u}^T]\!](t_{coh} - p_w\mathbf{n}_{\Gamma_d})d\Gamma = 0 \tag{14}$$

By integrating the product of Eq. (2) by the admissible test function ω' over the domain Ω, the weak form of the flow continuity equation can be obtained as:

$$\int_{\Omega} \left(\frac{\alpha-n}{K_s} + \frac{n}{K_w}\right)\dot{p}_w\omega' d\,\Omega + \int_{\Omega} \alpha\, \dot{\mathbf{u}}_{i,i}\omega' d\,\Omega + \int_{\Omega} \frac{1}{\rho_w}\left[\rho_w \frac{\mathbf{k}_{ij}}{\mu_w}\left(-p_{w,j} + \rho_w\mathbf{g}\right)\right]_{,i} \omega' d\,\Omega = 0 \tag{15}$$

Using the technique of integration by parts and applying the divergence theorem for discontinuous problems, the following equation is obtained:

$$\int_{\Omega} \left(\frac{\alpha-n}{K_s} + \frac{n}{K_w}\right)\dot{p}_w\omega' d\Omega + \int_{\Omega} \alpha\,\dot{u}_{i,i}\omega' d\Omega + \int_{\Gamma_{qw}} \frac{1}{\rho_w}\rho_w\frac{k_{ij}}{\mu_w}\left(-p_{w,j} + \rho_w g\right) n_{\Gamma}\omega' d\Gamma - \int_{\Gamma_d} \frac{1}{\rho_w}[\![\rho_w\frac{k_{ij}}{\mu_w}\left(-p_{w,j} + \rho_w g\right)\omega']\!] n_{\Gamma_d}d\Gamma - \int_{\Omega} \frac{1}{\rho_w}\left(\rho_w\frac{k_{ij}}{\mu_w}\left(-p_{w,j} + \rho_w g\right)\right)\omega'_{,i}d\Omega = 0 \tag{16}$$

Substituting relations $\omega' = \delta p_w$ and $\omega'_{,j} = \delta(Lp_w)$ into Eq. (16) and introducing boundary conditions (Eqs. (9) to (11)) into this equation results in the constrained Galerkin weak form of the flow continuity equation as follows:

$$\int_{\Omega} \delta p_w^T \left(\frac{\alpha-n}{K_s} + \frac{n}{K_w}\right)\dot{p}_w d\Omega + \int_{\Omega} \delta p_w^T \alpha\,\dot{u}_{i,i}d\Omega + \int_{\Gamma_{q_w}} \delta p_w^T\bar{q}_w d\Gamma - \int_{\Gamma_d} \delta p_w^T q_{Lw}d\Gamma' - \int_{\Omega} \delta\left(L_p p_w\right)^T \frac{k_{ij}}{\mu_w}\left(-p_{w,j}\right)d\Omega - \int_{\Omega} \delta\left(L_p p_w\right)^T \frac{k_{ij}}{\mu_w}(-\rho_w g)d\Omega + \delta\int_{\Gamma_{p_w}} \frac{1}{2}\left(p_w - \bar{p}_w\right)^T \alpha_{p_{pw}}\left(p_w - \bar{p}_w\right)d\Gamma = 0 \tag{17}$$

The fourth integral in Eq. (17) represents the mass transfer coupling between the fracture medium and the surrounding porous medium. This term can be obtained by applying the weighted residual method on the continuity equation for the fluid flow within the fracture (Eq. (3)) as:

$$\int_{\Omega'} \frac{1}{K_w}\dot{p}_w\omega' d\Omega + \int_{\Omega'} \frac{\dot{w}}{w}\omega' d\Omega' + \int_{\Omega'} \frac{1}{\rho_w}\left[\rho_w\overline{V}_{wi'}\right]_{,i'}\omega' d\Omega' = 0 \tag{18}$$

Where Ω' represents the discontinuity domain with a boundary Γ' as shown in Fig. 2. Note that the Integrals over the discontinuity domain are computed in the local coordinate system of the fracture (x', y', z), as shown in Fig. 2.

Applying the technique of integration by parts, using the Gauss-Green theorem, exploiting the momentum balance equation for the fluid flow within the fracture (Eq. (5)) and also Knowing that $\omega' = \delta p_w$ and $\omega'_{,j} = \delta\left(L''_p p_w\right)$, the above equation can be rewritten as follows:

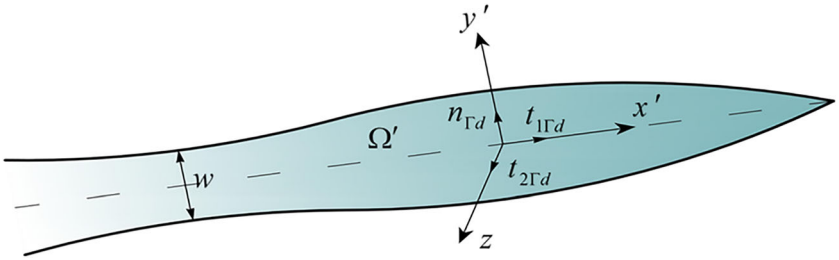

Fig. 2 The geometry of the discontinuity

$$\int_{\Omega'} \delta p_w^T \frac{1}{K_w} \dot{p}_w d\Omega' + \int_{\Omega'} \delta p_w^T \frac{\dot{w}}{w} d\Omega' + \int_{\Gamma_d} \delta p_w^T q_{L_w} d\Gamma' - \int_{\Omega'} \delta \left(L_p'' p_w\right)^T K_{wd} \left(-p_{w,i'}\right) d\Omega - \int_{\Omega'} \delta \left(L_p'' p_w\right)^T K_{wd} (\rho_w g) d\Omega' = 0 \tag{19}$$

Where L_p'' is the spatial differential operator for the fluid pressure variable within the fracture.

The fracturing fluid pressure variation across the fracture width can be disregarded, because the fracture width is negligible compared to its length and height. As a result, the first integral in Eq. (19) can be written as:

$$\int_{\Omega'} \delta p_w^T \frac{1}{K_w} \dot{p}_w d\Omega' = \int_{\Gamma_d} \int_{-w/2}^{w/2} \delta p_w^T \frac{1}{K_w} \dot{p}_w dy' d\Gamma' = \int_{\Gamma_d} \delta p_w^T \frac{w}{K_w} \dot{p}_w d\Gamma' \tag{20}$$

Since the crack width equals the difference between the normal components of the displacement vector, the second integral of Eq. (19) is written as:

$$\int_{\Omega'} \delta p_w^T \frac{\dot{w}}{w} d\Omega' = \int_{\Gamma_d} \int_{-w/2}^{w/2} \delta p_w^T \frac{\dot{w}}{w} dy' d\Gamma' = \int_{\Gamma_d} \delta p_w^T \dot{w} d\Gamma' = \int_{\Gamma_d} \delta p_w^T [\![\dot{\mathbf{u}}_y]\!] d\Gamma' \tag{21}$$

The distribution of fluid pressure is uniform across the fracture width, and as a result, the tangential derivatives of the fluid pressure with respect to y' remains constant. Therefore, the fourth integral in Eq. (19) is written as:

$$\int_{\Omega'} \delta \left(L_p'' p_w\right)^T K_{wd} \left(-p_{w,i'}\right) d\Omega' = \int_{\Gamma_d} \int_{-w/2}^{w/2} \delta \left(L_p'' p_w\right)^T K_{wd} \left(-p_{w,i'}\right) dy' d\Gamma' = \int_{\Gamma_d} \delta \left(L_p'' p_w\right)^T \frac{-1}{f} \frac{w^3}{12\mu_w} \left(L_p'' p_w\right) d\Gamma' \tag{22}$$

While the gravity acceleration is constant over the entire domain, the fifth integral in Eq. (19) can be written as:

$$\int_{\Omega'} \delta \left(L_p'' p_w\right)^T K_{wd} (\rho_w g_{i'}) d\Omega' = \int_{\Gamma_d} \int_{-w/2}^{w/2} \delta \left(L_p'' p_w\right)^T \frac{1}{f} \frac{w^3}{12\mu_w} \rho_w g_{i'} dy' d\Gamma' = \int_{\Gamma_d} \delta \left(\frac{\partial p_w}{\partial z}\right) \frac{1}{f} \frac{w^3}{12\mu_w} (\rho_w g_z) d\Gamma' \tag{23}$$

Introducing Eqs. (20) to (23) into Eq. (19), the mass transfer coupling term in Eq. (17) can be written as follows:

$$-\int_{\Gamma_d} \delta p_w^T q_{L_w} d\Gamma' = \int_{\Gamma_d} \delta p_w^T \frac{w}{K_w} \dot{p}_w d\Gamma' + \int_{\Gamma_d} \delta p_w^T [\![\dot{u}_y]\!] d\Gamma' - \int_{\Gamma_d} \delta \left(L_p'' p_w\right)^T \frac{-1}{f} \frac{w^3}{12\mu_w} \left(L_p'' p_w\right) d\Gamma' - \int_{\Gamma_d} \delta \left(\frac{\partial p_w}{\partial z}\right) \frac{1}{f} \frac{w^3}{12\mu_w} \rho_w g_z d\Gamma' \tag{24}$$

Substituting the mass transfer coupling term (Eq. (24)) into Eq. (17) results in the constrained Galerkin weak form of the flow continuity equation as follows:

$$\int_{\Omega} \delta p_w^T \left(\frac{\alpha - n}{K_s} + \frac{n}{K_w}\right) \dot{p}_w d\Omega + \int_{\Omega} \delta p_w^T \alpha \dot{u}_{i,i} d\Omega + \int_{\Gamma_{q_w}} \delta p_w^T \overline{q}_w d\Gamma + \int_{\Gamma_d} \delta p_w^T \frac{w}{K_w} \dot{p}_w d\Gamma' + \int_{\Gamma_d} \delta p_w^T [\![\dot{u}_y]\!] d\Gamma' - \int_{\Gamma_d} \delta \left(L_p'' p_w\right)^T \frac{-1}{f} \frac{w^3}{12\mu_w} \left(L_p'' p_w\right) d\Gamma' - \int_{\Gamma_d} \delta \left(\frac{\partial p_w}{\partial z}\right) \frac{1}{f} \frac{w^3}{12\mu_w} \rho_w g d\Gamma' - \int_{\Omega} \delta \left(L_p p_w\right)^T \frac{k_{ij}}{\mu_w} \left(-p_{w,j}\right) d\Omega - \int_{\Omega} \delta \left(L_p p_w\right)^T \frac{k_{ij}}{\mu_w} (\rho_w g) d\Omega + \delta \int_{\Gamma_{p_w}} \frac{1}{2} \left({}^{p_w}\alpha_{p_{pw}} \left(p_w - \overline{p}_w\right)\right) d\Gamma = 0 \tag{25}$$

Parameters α_u and $\alpha_{p_{pw}}$ denote the penalty factors for equilibrium and continuity of the pore fluid equations, respectively, and $\boldsymbol{\varepsilon}_{ii}$ is the volumetric strain of the soil skeleton. Spatial differential operators $\mathbf{L}$ and $\mathbf{L}_p$ are defined as follows:

$$\begin{aligned}\mathbf{L} &= \begin{bmatrix} \partial/\partial x & 0 & 0 & \partial/\partial y & 0 & \partial/\partial z \\ 0 & \partial/\partial y & 0 & \partial/\partial x & \partial/\partial z & 0 \\ 0 & 0 & \partial/\partial z & 0 & \partial/\partial y & \partial/\partial x \end{bmatrix}^T \\ \mathbf{L}_p &= [\partial/\partial x \partial/\partial y \partial/\partial z]^T \end{aligned} \tag{26}$$

2.4 Numerical discretization

In this section, spatial discretization of the governing partial differential equations is stated in the context of the enriched element-free Galerkin method. In order to capture the displacement jump across the fracture (strong discontinuity) and also the fluid flux jump normal to the fracture (weak discontinuity), it is necessary to enrich the displacement and pore fluid pressure fields by suitable functions discussed previously [33, 50, 62]. On this basis, the values of unknown variables of displacement and pore fluid pressure at any arbitrary point of the computational domain can be stated as follows:

$$\begin{aligned}\mathbf{u}^h(\mathbf{x}) &= \sum_{I=1}^{n_{std}} N_I^u(\mathbf{x})\,\mathbf{u}_I^{std} + \sum_{I=1}^{n_{enr}} N_I^u(\mathbf{x})\,\psi(\mathbf{x})\,\mathbf{u}_I^{enr} \\ p_w^h(\mathbf{x}) &= \sum_{I=1}^{n_{std}} N_I^p(\mathbf{x})\,(p_w)_I^{std} + \sum_{I=1}^{n_{enr}} N_I^p(\mathbf{x})\,\psi(\mathbf{x})\,(p_w)_I^{enr} \end{aligned} \tag{27}$$

In above equations, N_I^u and N_I^p indicate the standard MLS[3] shape functions associated with displacement and pore fluid pressure, respectively, and ψ is the enrichment function. As stated before, the Ridge and the Heaviside functions are employed as enrichment functions to simulate weak and strong discontinuities, respectively [50, 53]. n_{std} is the number of nodes in the support domain and n_{enr} denotes the number of enriched nodes in the neighborhood of the point of interest. Moreover, $\mathbf{u}_I^{enr}$ and $(p_w)_I^{enr}$ are enriched degrees of freedom. The selection of enriched nodes is performed by using the level set method as detailed in Ventura et al. [50] and Nguyen et al. [53].

The enhanced nodal shape functions and strain-deformation matrix ($\mathbf{B}$) for the field variable α can be stated as follows:

$$\begin{aligned}\mathbf{N}_I^{\alpha}(\mathbf{x}) &= \left[\mathbf{N}_I^{\alpha,std}(\mathbf{x})\mathbf{N}_I^{\alpha,enr}(\mathbf{x})\right] \\ \mathbf{B}_I^{\alpha}(\mathbf{x}) &= \left[\mathbf{B}_I^{\alpha,std}(\mathbf{x})\ \ \mathbf{B}_I^{\alpha,enr}(\mathbf{x})\right] \end{aligned} \tag{28}$$

$\mathbf{N}^{enr}$ and $\mathbf{B}^{enr}$ are the enriched parts of the enhanced shape function and $\mathbf{B}$ matrix, respectively, as follows. Note that the function ψ in the above equations can be either the Ridge $R(x)$ or the Heaviside $H(x)$ functions, depending on the type of discontinuity.

$$N_I^{\alpha,enr} = N_I^{\alpha,std}\psi$$

$$\mathbf{B}_I^{u,enr} = \begin{bmatrix} \frac{\partial N_I^{u,std}}{\partial x}\psi + \frac{\partial \psi}{\partial x}N_I^{u,std} & 0 & 0 \\ 0 & \frac{\partial N_I^{u,std}}{\partial y}\psi + \frac{\partial \psi}{\partial y}N_I^{u,std} & 0 \\ 0 & 0 & \frac{\partial N_I^{u,std}}{\partial z}\psi + \frac{\partial \psi}{\partial z}N_I^{u,std} \\ \frac{\partial N_I^{u,std}}{\partial y}\psi + \frac{\partial \psi}{\partial y}N_I^{u,std} & \frac{\partial N_I^{u,std}}{\partial x}\psi + \frac{\partial \psi}{\partial x}N_I^{u,std} & 0 \\ 0 & \frac{\partial N_I^{u,std}}{\partial z}\psi + \frac{\partial \psi}{\partial z}N_I^{u,std} & \frac{\partial N_I^{u,std}}{\partial y}\psi + \frac{\partial \psi}{\partial y}N_I^{u,std} \\ \frac{\partial N_I^{u,std}}{\partial z}\psi + \frac{\partial \psi}{\partial z}N_I^{u,std} & 0 & \frac{\partial N_I^{u,std}}{\partial x}\psi + \frac{\partial \psi}{\partial x}N_I^{u,std} \end{bmatrix} \tag{29}$$

$$B_I^{p,enr} = \begin{bmatrix} \frac{\partial N_I^{p,std}}{\partial x}\psi + \frac{\partial \psi}{\partial x}N_I^{p,std} \\ \frac{\partial N_I^{p,std}}{\partial y}\psi + \frac{\partial \psi}{\partial y}N_I^{p,std} \\ \frac{\partial N_I^{p,std}}{\partial z}\psi + \frac{\partial \psi}{\partial z}N_I^{p,std} \end{bmatrix}$$

[3] Moving Least Square

Using Eq. (29), the matrix form of a fully coupled set of hydro-mechanical governing equations for the simulation of the hydraulic fracture process can be obtained as follows:

$$\begin{aligned}\left(C_{11}+C_u^{\alpha}\right)U-(C_{12}+C_{12cr})p_w &= F_u+F_u^{\alpha}-F_{\Gamma d}\\ &\quad (C_{21}+C_{21cr})\dot{U}\\ +(C_{22}+C_{22cr})\dot{p_w}+\left(K_{22}+K_{22cr}+K_{p_w}^{\alpha}\right)p_w&\\ =F_{p_w}+F_{p_w}^{\alpha}+F_{p_wcr}^{\alpha}&\end{aligned} \tag{30}$$

The superscript $(\cdot)$ stands for the temporal derivative. The vectors and matrices presented in Eq. (30) can be calculated numerically by assembling nodal vectors and matrices given in the Appendix. To achieve this goal, the gauss quadrature integration technique is employed to numerically compute the vectors and matrices.

2.5 Solution procedure

Since the resulting system of fully coupled algebraic equations is highly nonlinear, a suitable strategy should be employed to linearize the system of equations. For this purpose, the Newton-Raphson iterative algorithm is implemented in this study. Assuming a linear variation for derivatives of unknown variables in time and employing the fully implicit finite difference technique for temporal discretization, the residual forms of Eq. (30) can be written as:

$$\begin{aligned}R_u^{i,n+1}&=\left(C_{11}+C_u^{\alpha}\right)U^{i,n+1}-(C_{12}+C_{12cr})p_w^{i,n+1}-F_u^{n+1}-F_u^{\alpha\ n+1}+F_{\Gamma_d}^{i,n+1}\\ R_{p_w}^{i,n+1}&=(C_{21}+C_{21\,cr})\frac{U^{i,n+1}-U^n}{\Delta t}+(C_{22}+C_{22cr})\frac{p_w^{i,n+1}-p_w^n}{\Delta t}+\left(K_{22}+K_{22cr}+K_{p_w}^{\alpha}\right)p_w^{i,n+1}-F_{p_w}^{n+1}-F_{p_w}^{\alpha\ n+1}\end{aligned} \tag{31}$$

Where Δt denotes the time step. Expanding the residual equations with the first-order truncated Taylor series, the following equation can be obtained:

$$R^{i+1,n+1}=R^{i,n+1}+J\left[dX^{i+1,n+1}\right]=0 \tag{32}$$

Where $dX^{i+1,\ n+1}$ denotes the unknown increment and J is the Jacobian matrix which is obtained by differentiating the residual matrix with respect to the unknown matrix as:

$$\begin{aligned}J&=\begin{bmatrix}\frac{\partial R_u}{\partial U} & \frac{\partial R_u}{\partial p_w}\\ \frac{\partial R_{p_w}}{\partial U} & \frac{\partial R_{p_w}}{\partial p_w}\end{bmatrix}\\ &=\begin{bmatrix}\left(C_{11}+C_u^{\alpha}\right)+K_{\Gamma d} & -(C_{12}+C_{12cr})\\ \frac{C_{21}+C_{21cr}}{\Delta t} & \frac{C_{22}+C_{22cr}}{\Delta t}+K_{22}+K_{22cr}+K_{p_w}^{\alpha}\end{bmatrix}\end{aligned} \tag{33}$$

Solving Eq. (32), the unknown increment vector can be obtained as follows:

$$\left[dX^{i+1,n+1}\right]=\begin{bmatrix}dU^{i+1,n+1}\\ dp_w^{i+1,n+1}\end{bmatrix}=-J^{-1}R^{i,n+1} \tag{34}$$

Where $R^{i,\ n+1}$ is computed as:

$$R^{i,n+1}=J\begin{bmatrix}U^{i,n+1}\\ P_w^{i,n+1}\end{bmatrix}-\begin{bmatrix}\left(F_u+F_u^{\alpha}\right)^{n+1}\\ \left(F_{pw}+F_{pw}^{\alpha}+F_{\boldsymbol{pwcr}}{}^{\alpha}\right)^{n+1}\end{bmatrix}-P^n \tag{35}$$

And P^n is a vector that is computed from the converged solution of the last time step of analysis:

$$P^n=\begin{Bmatrix}0\\ (C_{21}+C_{21cr})\frac{U^n}{\Delta t}+(C_{22}+C_{22cr})\frac{P_w^n}{\Delta t}\end{Bmatrix} \tag{36}$$

Finally, the unknown vector is obtained at new iteration of the current time step until the desired convergence criterion is satisfied:

$$X^{i+1,n+1}=X^{i,n+1}+dX^{i+1,n+1} \tag{37}$$

Following this procedure, a perfect convergence with a tolerable error was seen in all computations.

3 Enriched EFG method

In this section, the principles of the enriched EFG method are briefly explained. Element-free Galerkin method is one of the commonly used mesh-less methods for the simulation of a broad range of problems in solid mechanics, including crack growth problems. In this method, to construct shape functions, the Moving Least Square (MLS) procedure is used, which is a combination of two components of the weight function and the basis function. In this paper, cubic spline weight function (Eq. (38)) and a linear polynomial basis (Eq. (39)) are employed for creating MLS shape functions [36] as follows:

$$\widehat{W}(\mathbf{x}-\mathbf{x}_I)\equiv\widehat{W}(r)=\begin{cases}\frac{2}{3}-4r^2+4r^3 & r\le\frac{1}{2}\\ \frac{4}{3}-4r+4r^2-\frac{4}{3}r^3 & 1<r<\frac{1}{2}\\ 0 & r\ge 1\end{cases} \tag{38}$$

$$P^T(\mathbf{x})=P^T(x,y,z)=\{1,x,y,z\} \tag{39}$$

In Eq. (38), $r=\|\mathbf{x}-\mathbf{x}_I\|/(R_{id})_I$, where $\|\mathbf{x}-\mathbf{x}_I\|$ is the distance between the evaluation point and node I and $(R_{id})_I$ is the radius of the influence domain of the *Ith* node. As the MLS shape functions lack the Kronecker delta property, the imposition of essential boundary conditions is not as simple as the finite element method, and a proper strategy must be adopted for this purpose. Between the penalty and Lagrange multipliers methods, the penalty method is employed in this study for the imposition of the essential boundary conditions [36]. By exploiting the partition of unity property of MLS shape functions, the extrinsic enrichment strategy is used to simulate weak and strong discontinuities [33, 50, 62]. In this regard, the field variables along the line/surface of the discontinuity must be enriched by proper functions to reproduce the desired properties. For strong discontinuities, the *Heaviside* enrichment function is used as follows:

$$H(\mathbf{x})=\begin{cases}-1 & \text{if } \varphi(\mathbf{x})<0\\ +1 & \text{if } \varphi(\mathbf{x})\ge 0\end{cases} \tag{40}$$

Also, in the case of weak discontinuities, the *Ramp* or *Ridge* enrichment functions can be employed [58]. In this study, The *Ridge* function is used for the simulation of weak discontinuities, as follows:

$$R(\mathbf{x})=\sum_{I\in n^{enr}}N_I(\mathbf{x})|\varphi_I|-\left|\sum_{I\in n^{enr}}N_I(\mathbf{x})\varphi_I\right| \tag{41}$$

This enrichment function eliminates the low accuracy due to the existence of blending supporting domains [22, 63]. In Eqs. (40) and (41), the function φ is the *signed distance function* which is the most commonly used level set function to represent the line/surface of the discontinuity [50, 53, 58]:

$$\varphi(\mathbf{x})=\|\mathbf{x}-\mathbf{x}^*\|\ \text{sign}\ \left(\mathbf{n}_{\Gamma_d}\cdot(\mathbf{x}-\mathbf{x}^*)\right) \tag{42}$$

Where $\mathbf{x}^*$ denotes the closest point on the discontinuity Γ_d from the point $\mathbf{x}$; $\mathbf{n}_{\Gamma_d}$ is the unit normal vector to the interface at $\mathbf{x}^*$; and $\|\mathbf{x}-\mathbf{x}^*\|$ represents the distance of the point $\mathbf{x}$ to the discontinuity. Also, N_I and n^{enr} in Eq. (41) denote the standard MLS shape function and the number of nodes whose supports intersect the line/surface of the discontinuity, respectively.

4 Cohesive crack model

It is proven that linear elastic fracture mechanics is applicable in crack growth problems when the length of the damaged zone ahead of the crack tip is negligible in comparison to the crack length. In such cases, the stress field at the crack tip is highly singular, and theoretically, the stress at the fracture tip tends to infinity. On the other hand, in quasi-brittle materials such as concrete and geomaterials, the nonlinear zone in front of the crack tip (called the fracture process zone) is not negligible, due to plasticity and micro-cracking. In these materials, the stress amount ahead of the crack tip is limited to a certain value which is the tensile strength of the materials [58]. On this basis, Barenblatt [64] introduced the cohesive crack model to describe the near-tip nonlinear processes in quasi-brittle materials and to eliminate the tip singularity assumption, which is an unrealistic assumption of linear elastic fracture mechanics. The nonlinear behavior of materials in the cohesive crack model is specified by cohesive tractions transmitted at the fracture edges across the fracture process zone. The magnitude of cohesive tractions ($\mathbf{t}_{coh}$) at any point of the fracture process zone is proportional to the fracture opening (displacement jump) that is characterized by a proper traction-separation law which is also known as cohesive constitutive relation as follows [58]:

$$\mathbf{t}_{coh}=\mathbf{t}_{coh}(\llbracket\mathbf{u}\rrbracket) \tag{43}$$

Where $\llbracket\mathbf{u}\rrbracket$ is defined as the displacement jump across the discontinuity or fracture aperture. From Eq. (27), the displacement field can be written as follows:

$$\mathbf{u}=N^s\mathbf{u}^s+N^e\mathbf{u}^e \tag{44}$$

Recall that the enriched shape function can be obtained by multiplying the standard shape function and the enrichment function, and using the Heaviside function (Eq. (40)) as the

enrichment function for the displacement field, the following relation can be obtained:

$$H = \begin{cases} +1 \ \text{ if } \ \phi(x) \geq 0 \\ -1 \ \text{ if } \ \phi(x) < 0 \end{cases} \rightarrow \begin{cases} N^{e+} = N^s H = N^s \\ N^{e-} = N^s H = -N^s \end{cases} \tag{45}$$

Using Eqs. (44) and (45), the displacement jump (fracture aperture) can be calculated as follows:

$$\begin{aligned} [\![\mathbf{u}]\!] &= \mathbf{u}^+ - \mathbf{u}^- = (N^s \mathbf{u}^s + N^s \mathbf{u}^e) - (N^s \mathbf{u}^s - N^s \mathbf{u}^e) \\ &= 2N^s \mathbf{u}^e \end{aligned} \tag{46}$$

Where superscripts "+" and "- "indicate the value of a parameter at any side of the fracture. In this study, a linear cohesive constitutive relation is used, as shown in Fig. 3.

In this figure, f_t is the tensile strength and ω_c denotes critical opening displacement over which cohesive traction is zero. The closing area under the traction-displacement curve represents the fracture energyG_f, which is a material property.

By linearization of Eq. (43), the differential form of the traction-separation law can be obtained as follows:

$$\mathrm{d}\mathbf{t}_{coh} = \mathbf{D}_{coh} \mathrm{d}[\![\mathbf{u}]\!] \tag{47}$$

Where $\mathbf{D}_{coh}$ is the tangential modulus matrix of the discontinuity. In the case of mode *I*failure and by neglecting the tangential components of the cohesive tractions vector, the linear traction-separation relation can be written as follows:

$$\mathbf{t}_{coh} = \frac{-f_t^2}{2G_f}\omega + f_t \tag{48}$$

Hence, the tangential modulus matrix of the discontinuity in the cohesive crack model can be simplified as follows:

$$\mathbf{D}_{coh} = \mathbf{n}_{\Gamma_d} \frac{-f_t^2}{2G_f} \mathbf{n}_{\Gamma_d}^T \tag{49}$$

In Eq. (49), $\mathbf{n}_{\Gamma_d}$ is the unit normal vector to the discontinuity. It should be noted that exceeding the normal stress at the crack tip from the tensile strength of the material is defined as the crack propagation criteria.

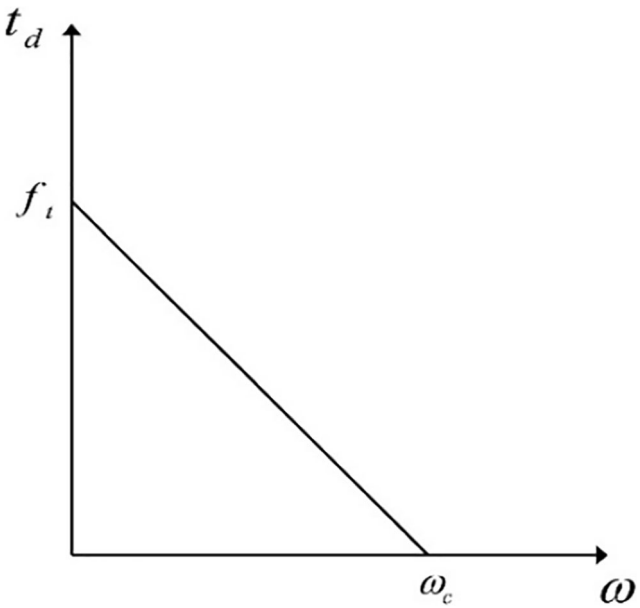

Fig. 3 The linear cohesive traction-separation law used in this study

5 Numerical simulation results

5.1 Verification

The purpose of this section is to validate the developed computational algorithm and to demonstrate the capability of the proposed enriched EFG framework in the simulation of hydraulic fracturing problems. To achieve this goal, the propagation of a vertical hydraulic fracture in an infinite saturated porous medium is considered. In this example, a viscous Newtonian fluid is pumped at a constant flow rate to hydraulically propagate a vertical fracture in an infinite saturated porous medium. The analytical solution to this problem was presented first by Geertsma and De Klerk [5], assuming incompressible fluid and impermeable porous medium, as follows:

$$\begin{aligned} CMOD &= 1.87\left(\frac{\mu(1-\nu)Q^3}{H^3 G}\right)^{\frac{1}{6}} t^{\frac{1}{3}} \\ L &= 0.65\left(\frac{GQ^3}{\mu(1-\nu)H^3}\right)^{\frac{1}{6}} t^{\frac{2}{3}} \\ CMP &= \frac{1.97}{H}\left(\frac{G^3 Q\mu H^3}{(1-\nu)^3 L^2}\right)^{\frac{1}{4}} + S \end{aligned} \tag{50}$$

CMOD is the crack mouth opening displacement and *CMP* denotes the crack mouth pressure. L and H denote the crack length and height, respectively. Also, μ is the fluid viscosity, G is the shear modulus, ν is the Poisson's ratio, Q is the injection rate, t is time and S denotes the in-situ stress normal to the crack propagation direction. Figure 4 displays the geometry and boundary conditions considered for the numerical

simulation of this problem using the proposed enriched EFG method. The material properties are shown in Table 1.

The in-situ stress is considered to be zero and the gravitational effects are disregarded. In addition, the initial pore fluid pressure is equal to the atmospheric pressure and assumed to be zero. In order to perform a more precise comparison between the numerical and analytical solution, the intrinsic permeability of the host rock assumed to be $6md$ which is equivalent to the permeability of $k = 6 \times 10^{-15} m^2$ and the fracturing fluid is considered to be incompressible [23].

The EFG nodal pattern considered in this problem is shown in Fig. 5. In order to obtain precise results for pressure distribution and accurately capture the cohesive tractions along the fracture process zone, the arrangement of nodes around the crack path is considered to be dense. The background mesh with hexahedral elements which is used for integration purposes, is shown in Fig. 6.

The fracturing fluid is injected into a $0.1m$ long initial crack at a constant rate of $Q = 0.0001 m^2/s$. The fracturing process is modeled using the cohesive crack concept, and the nonlinear behavior of the material at the fracture process zone is simulated by a linear softening cohesive law with the parameters of $f_t = 0.45\ MPa$ and $G_f = 143\ N/m$ [23]. Because of symmetry, the hydraulic fracture propagates under mode I, which is an opening mode. In this mode, the crack faces separate symmetrically with respect to the crack front so that the displacements of the crack surfaces are perpendicular to the crack plane. Numerical simulation results, including the variation of crack length, crack mouth opening displacement, and crack mouth pressure, are presented in Figs. 7, 8, 9 and compared with the analytical solution presented by Geertsma and De Klerk [5] and also the extended finite element method [23].

Table 1 Material properties [23]

Property	Value	Unit
Initial porosity	0.19	–
Fluid dynamic viscosity	0.001	Pa. s
Fluid phase density	1000	kg/m^3
Solid phase density	1000	kg/m^3
Elastic young modulus	15960	kPa
Poison's ratio	0.33	–
Biot coefficient	0.79	–
Fluid phase bulk modulus	3000	MPa
Solid phase bulk modulus	36000	MPa

The good agreement between numerical and analytical solutions shows that the proposed numerical framework can accurately simulate the process of hydraulic fracturing in saturated porous media. Figure 9 shows that as the injection process starts, the crack mouth pressure falls suddenly and then follows a gradual decrease with time. The difference between XEFG and analytical results for the crack mouth pressure originates from the fact that the basic assumptions of the analytical solution proposed by Geertsma and de Klerk [5] are incompressible fluid and impermeable porous medium. Although the intrinsic permeability considered for numerical simulation is relatively low, the medium is not completely impermeable. Hence, the fluid leak-off from the fracture medium into the surrounding porous rock results in a lower crack mouth pressure than the analytical solution. In addition, although the crack mouth pressures predicted by the XFEM are different from the values of the XEFG method in the initial time steps, the values of the two methods gradually approach each other.

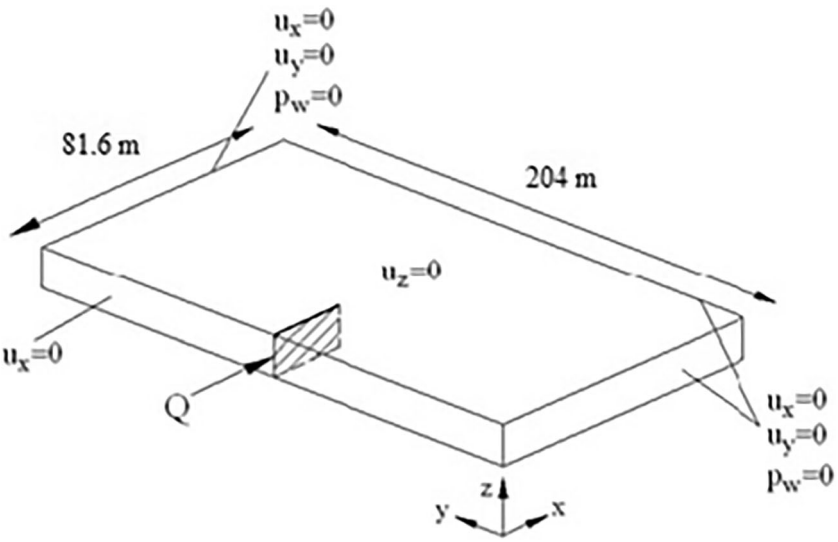

Fig. 4 Geometry and boundary conditions of the hydraulic fracturing problem

Fig. 5 Nodal arrangement

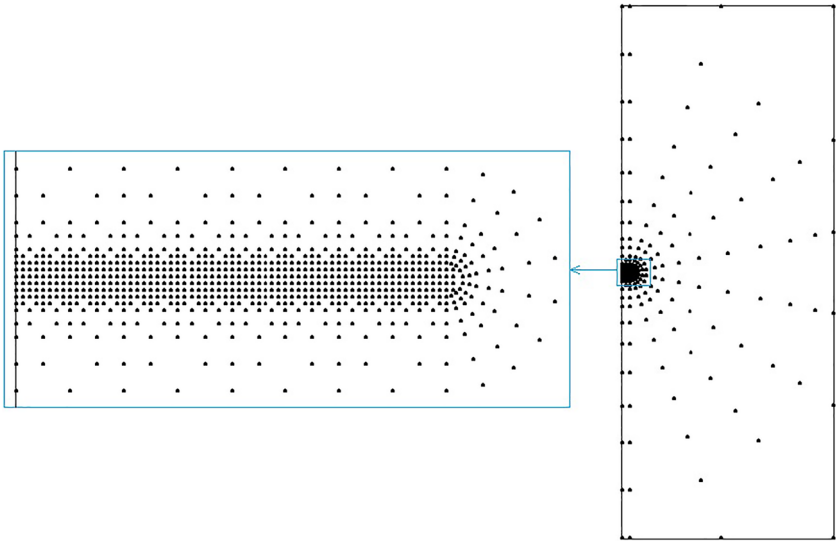

Figure 10 demonstrates the contours of pore fluid pressure and vertical displacement in the vicinity of hydro-fracture at 1, 3, and 5 seconds from the beginning of injection. The propagation of fracture can be seen from the temporal variation of fluid pressure in the vicinity of hydro-fracture along with the distribution of vertical displacement. Variations of fluid pressure within the fracture and the crack opening at three different times of 1, 3, and 5 seconds are presented in Fig. 11. As can be seen, the fracturing fluid pressure along the fracture decreases gradually and reaches a negative value at the vicinity of the crack tip, then tends to the initial pore fluid pressure of the medium. The distance between the crack tip and the fracturing fluid front (where the fracturing fluid pressure sign changes), which is called the fluid–lag zone [65], is modeled accurately, as shown in Fig. 11.

Also, the variations of crack opening along the fracture at three different times are shown in this figure.

Other verification examples can be found elsewhere [63].

Fig. 6 Background mesh

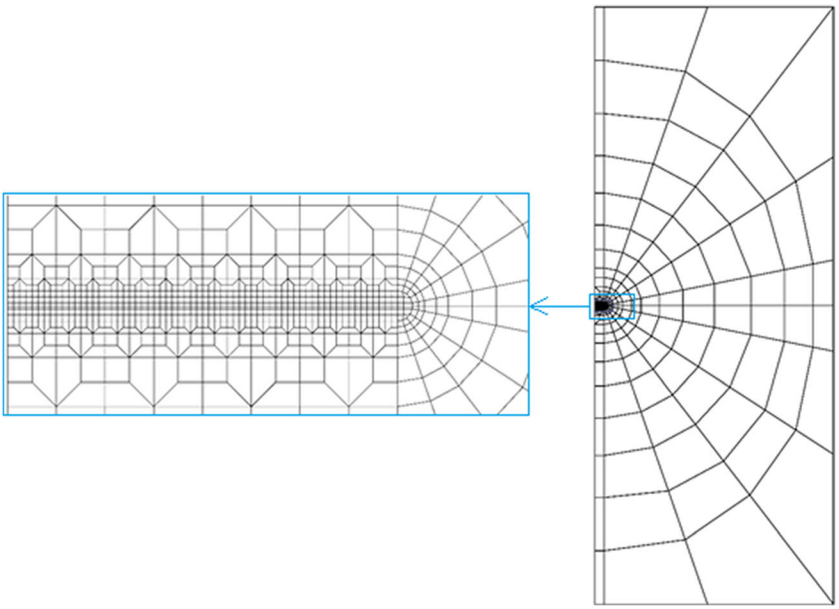

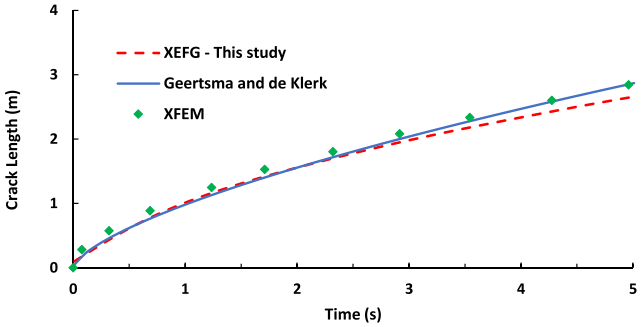

Fig. 7 Variation of the crack length with time

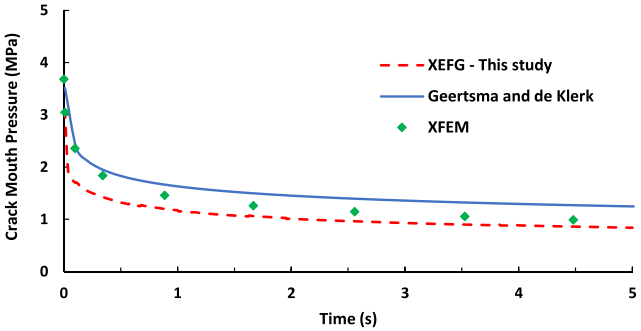

Fig. 9 Variation of the crack mouth pressure with time

5.2 Parametric analysis

In the next stage, the effects of some parameters such as permeability coefficient, injection rate, and fluid viscosity on the crack length, crack mouth opening displacement, and the crack mouth pressure are investigated. Figures 12, 13, and 14 show the time variation of the aforementioned characteristics of the fracture in relation to different amounts of intrinsic permeability of the surrounding porous medium. By increasing the intrinsic permeability, the leak-off of the fracture fluid into the surrounding porous rock increases, and the pressure applied onto the crack walls (including the crack mouth) by means of the fracturing fluid decreases. As a result, the hydro-fracture propagates slower and the crack mouth opening displacement decreases accordingly. On the other hand, by increasing the intrinsic permeability, a higher injection pressure is needed to propagate the hydraulic fracture. This decrease and increase in crack mouth pressure compensate for each other and as a result, the crack mouth pressure is not affected considerably by the intrinsic permeability of the porous rock, as depicted in Fig. 14.

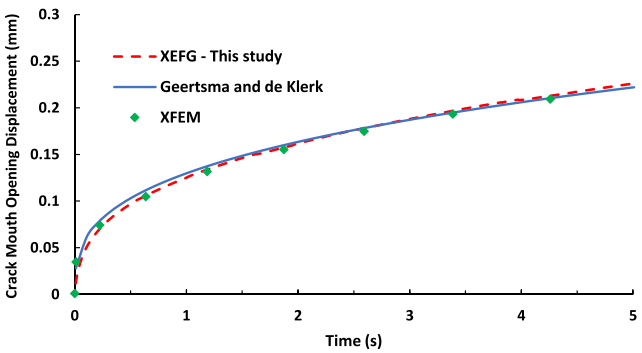

Fig. 8 Variation of the crack mouth opening displacement with time

The effects of injection rate on the crack length, crack mouth opening displacement, and the crack mouth pressure are presented in Figs. 15, 16 and 17. These figures show that by increasing the fluid injection rate, the crack length and the crack mouth opening displacement increase. However, by increasing the injection rate, the required fluid pressure for crack propagation is reduced. On the other hand, the fluid pressure at the crack mouth tends to increase by increasing the injection rate. Therefore, this decrease and increase in fluid pressure at the crack mouth cancel each other, and as a result, the injection rate variation doesn't affect the crack mouth pressure considerably, as shown in Fig. 17.

Figures 18, 19 and 20 demonstrate the variation of crack length, crack mouth opening displacement, and crack mouth pressure with time, for different values of dynamic viscosities. Increasing the dynamic viscosity decreases Darcy's permeability and also decreases the permeability of fracture medium according to the cubic law. As a result, increasing the dynamic viscosity, reduces the propagation velocity and increases the crack mouth opening displacement. In addition, by increasing the fluid dynamic viscosity, the required injection pressure for the propagation of hydro-fracture becomes greater.

6 Conclusion

A comprehensive numerical simulation of the multi-physics process of hydraulic fracturing requires considering several components, including fluid flow within the fracture as well as the host medium, fluid leak-off, rock deformations, and crack propagation. On this basis, in the present study, a fully coupled extrinsically enriched element-free Galerkin software was developed, in order to simulate the propagation of hydraulically driven fractures. To describe the nonlinear behavior of the material along the fracture process zone, the

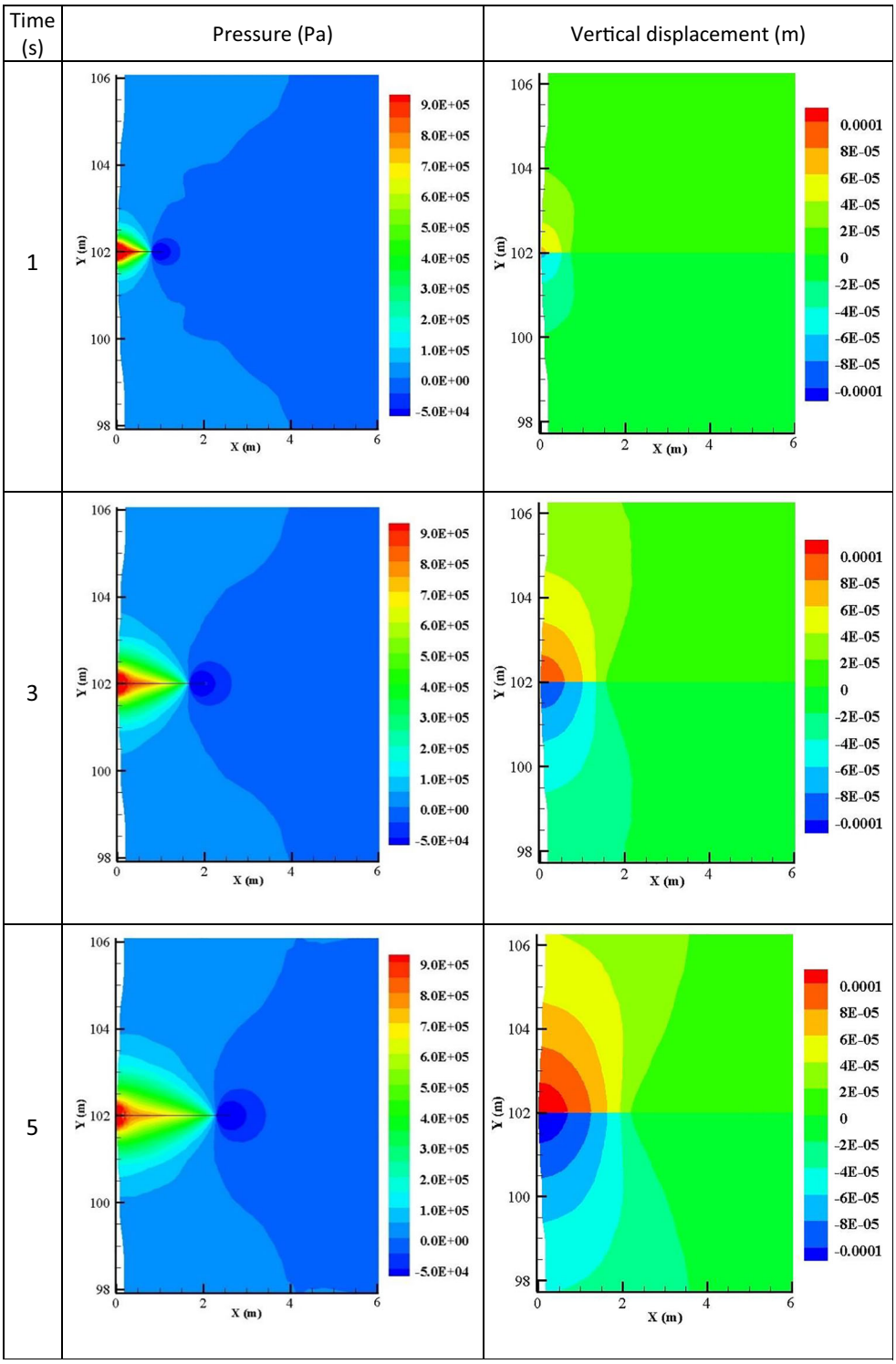

Fig. 10 Contours of fluid pressure and vertical displacement at three different times

cohesive crack model was employed. The fracturing fluid flow within the fracture medium was modeled using the lubrication theory, and the permeability of the fracture was calculated using cubic law. Contrary to analytical solutions and some of the numerical models, the rock matrix surrounding the fracture is considered a porous deformable medium and the fluid leak-off phenomenon as well as the formation of the fluid-lag zone in front of the fracture are successfully simulated. Numerical simulation results showed that the proposed algorithm based on the enriched EFG method can accurately predict different aspects of the hydraulic fracturing process in saturated deformable porous media.

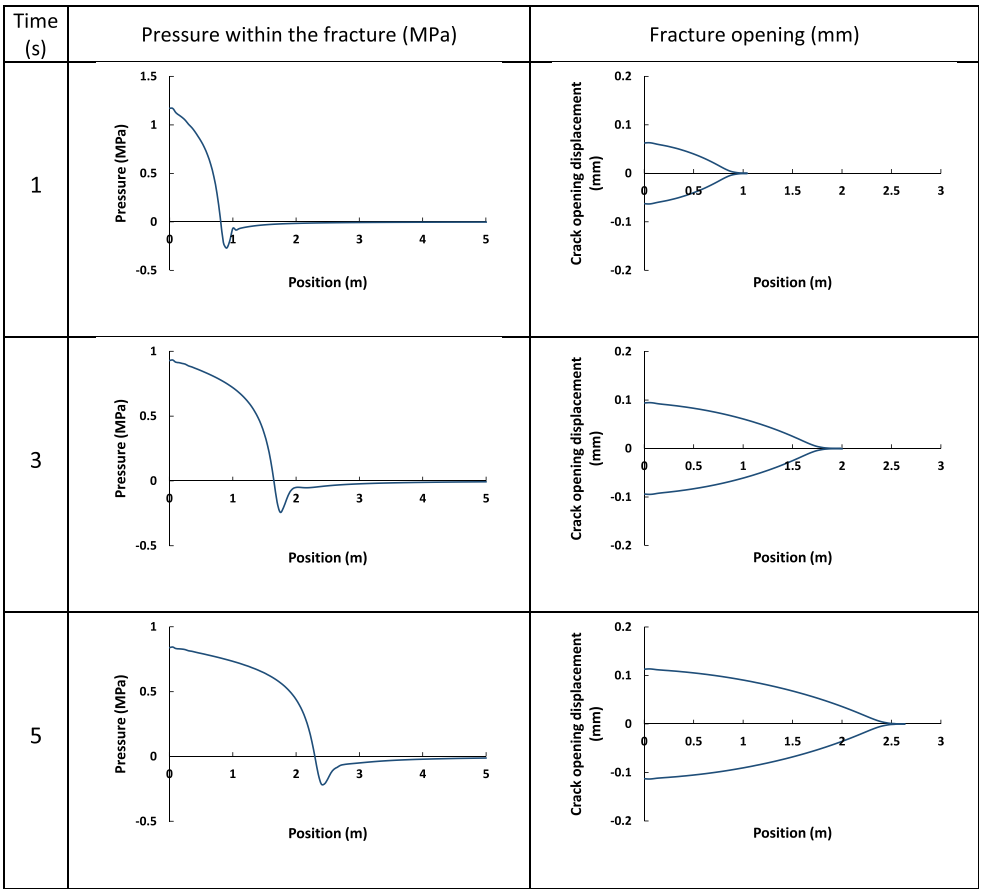

Fig. 11 Variation of fluid pressure within the fracture and fracture opening at three different times

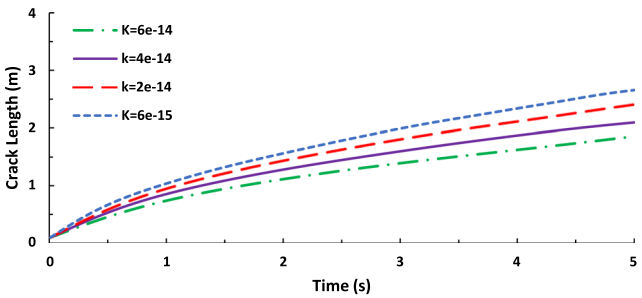

Fig. 12 Time variation of the crack length for different intrinsic permeabilities of porous rock (m^2)

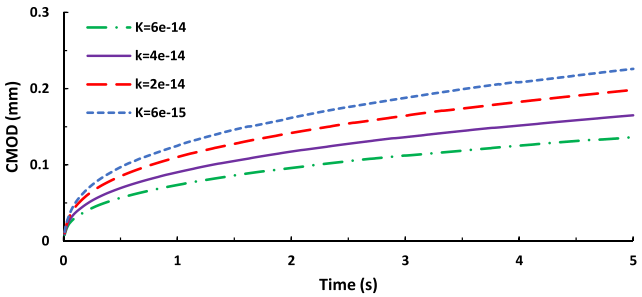

Fig. 13 Time variation of the CMOD for different intrinsic permeabilities of porous rock (m^2)

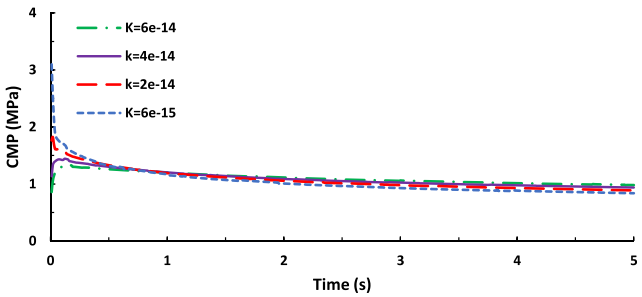

Fig. 14 Time variation of the CMP for different intrinsic permeabilities of porous rock (m^2)

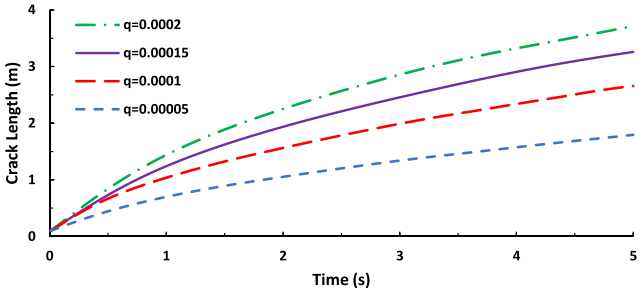

Fig. 15 Time variation of the crack length for different injection rates (m^2/s)

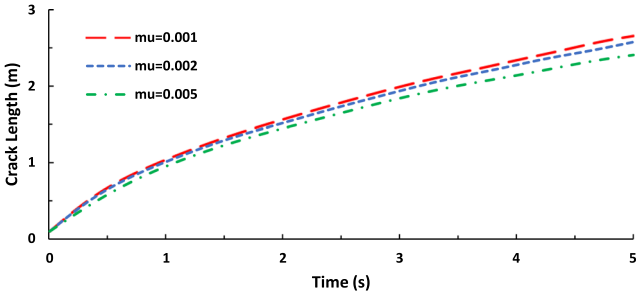

Fig. 18 Time variation of the crack length for different dynamic viscosities (Pa.s)

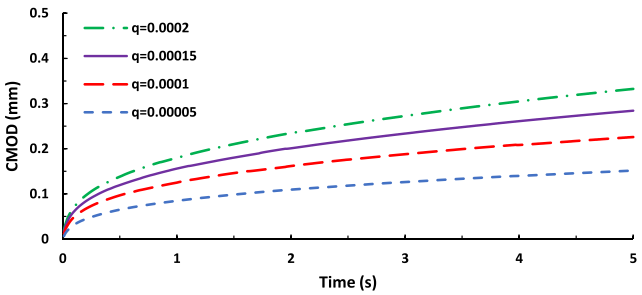

Fig. 16 Time variation of the crack mouth opening displacement for different injection rates (m^2/s)

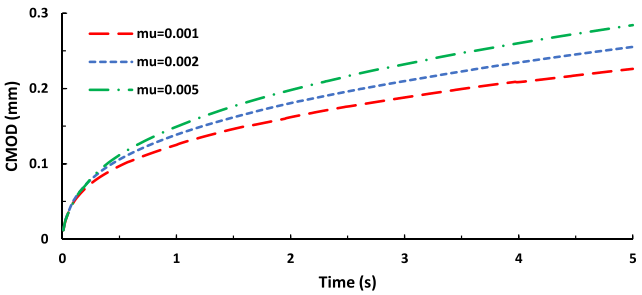

Fig. 19 Time variation of the crack mouth opening displacement for different dynamic viscosities (Pa.s)

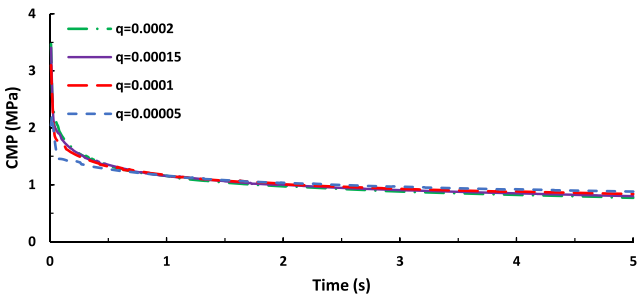

Fig. 17 Time variation of the crack mouth pressure for different injection rates (m^2/s)

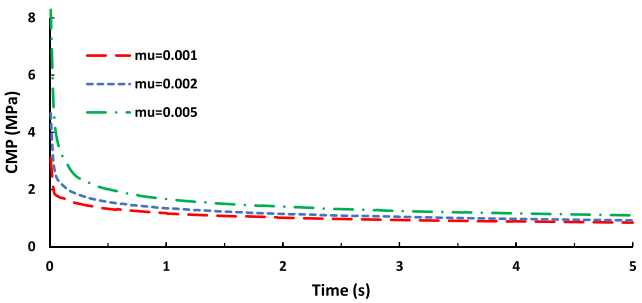

Fig. 20 Time variation of the crack mouth pressure for different dynamic viscosities (Pa.s)

Appendix

The nodal vectors and matrices in Eq. (30) are defined as:

$$C_{11} = \int_{\Omega} B^T D B d\Omega$$

$$C_{12} = \int_{\Omega} B^T \alpha \delta_{ij} N d\Omega$$

$$F_u = \int_{\Gamma_t} N^T \bar{t} d\Gamma + \int_{\Omega} N^T \rho g_i d\Omega$$

$$F_{\Gamma_d} = \int_{\Gamma_d} N^T t_d d\Gamma'$$

$$C_{21cr} = 2 \int_{\Gamma_d} N_p^T n_{\Gamma_d}^T N d\Gamma'$$

$$C_{22cr} = \int_{\Gamma_d} N_p^T \frac{w}{K_w} N_p d\Gamma'$$

$$K_{22cr} = \int_{\Gamma_d} B_p^T t_{\Gamma_d}^T \frac{1}{f} \frac{w^3}{12\mu_w} t_{\Gamma_d} B_p d\Gamma'$$

$$F_{p_w} = \int_{\Omega} B_p^T \frac{k_{ij}}{\mu_w} \rho_w g d\Omega - \int_{\Gamma_{qw}} N_p^T \bar{q}_w d\Gamma$$

$$F_{p_{wcr}} = \int_{\Gamma_d} B_p^T t_{\Gamma_d}^T \frac{1}{f} \frac{w^3}{12\mu_w} \rho_w g_i d\Gamma'$$

$$C_u^{\alpha} = \int_{\Gamma_u} N^T \alpha_{p_u} N d\Gamma$$

$$C_{12cr} = 2 \int_{\Gamma_d} N^T n_{\Gamma_d} N d\Gamma'$$

$$F_u^{\alpha} = \int_{\Gamma_u} N^T \alpha_{p_u} \bar{u} d\Gamma$$

$$C_{21} = \int_{\Omega} N_p^T \alpha m^T B d\Omega$$

$$C_{22} = \int_{\Omega} N_p^T \left(\frac{\alpha - n}{K_s} + \frac{n}{K_w} \right) N_p d\Omega$$

$$K_{22} = \int_{\Omega} B_p^T \frac{k_{ij}}{\mu_w} B_p d\Omega$$

$$K_{p_w}^{\alpha} = \int_{\Gamma_{pw}} N_p^T \alpha_{p_{pw}} N_p d\Gamma$$

$$F_{p_w}^{\alpha} = \int_{\Gamma_{pw}} N_p^T \alpha_{p_{pw}} \bar{p}_w d\Gamma$$

Nomenclature $\mathbf{D}_{coh}$, Tangential modulus matrix of the discontinuity; $\mathbf{D}_{Tijkl}$, Fourth-order tangential stiffness tensor; f_t, Tensile strength; f, Roughness coefficient; G_f, Fracture energy; $\mathbf{g}_i$, Acceleration of gravity vector; H, Heaviside enrichment function; J, Jacobian matrix; K_s, bulk moduli of the solid grains; K_T, bulk moduli of the porous skeleton; K_w, bulk moduli of the fluid phase; $\mathbf{k}_{ij}$, Tensor of intrinsic permeability; n, Porosity; $\mathbf{n}_i$, Outward unit vector normal to the external boundary; $\mathbf{n}_{\Gamma_d}$, Unit normal vector to the discontinuity line/surface; N^{std}, Standard shape function; N^{enr}, Enriched shape function; p_w, Pore fluid pressure; R, Ridge enrichment function; t, Time; $\bar{\mathbf{t}}_i$, traction force; t_{coh}, cohesive tractions; $\mathbf{u}$, Solid displacement vector; $\dot{\mathbf{u}}^{ws}{}_i$, Relative velocity vector between the fluid phase and solid phase; $\bar{\mathbf{v}}_{wi}$, Average velocity vector of the injected fluid; w, Fracture aperture; α, Biot's parameters; δ_{ij}, Kronecker delta; ε_{kl}, Strain tensor; μ_w, Dynamic viscosity of pore fluid; ρ, Average density of the mixture; ρ_s, Solid density; ρ_w, Pore fluid density; σ_{ij}, Total stress tensor; $\varphi(\mathbf{x})$, Signed distance function; ψ, Enrichment function; ω_c, critical opening displacement

Data availability Some or all data, models, or codes that support the findings of this study are available from the corresponding author upon reasonable request.

Declarations

Competing interests The authors declare that they have no competing financial interests that could have appeared to influence the work reported in this paper.

References

1. Li, Q., Xing, H., Liu, J., Liu, X.: A review on hydraulic fracturing of unconventional reservoir. Petroleum. **1**, 8–15 (2015)
2. Nilsson, B., Tzovolou, D., Jeczalik, M., Kasela, T., Slack, W., Klint, K.E., Haeseler, F., Tsakiroglou, C.D.: Combining steam injection with hydraulic fracturing for the in situ remediation of the unsaturated zone of a fractured soil polluted by jet fuel. J. Environ. Manag. **92**, 695–707 (2011). https://doi.org/10.1016/j.jenvman.2010.10.004
3. Kumari WGP, Ranjith PG, Perera MSA, Li X, Li LH, Chen BK, et al. Hydraulic fracturing under high temperature and pressure conditions with micro CT applications : Geothermal energy from hot dry rocks 2018;230:138–154. https://doi.org/10.1016/j.fuel.2018.05.040
4. Khristianovic, S., Zheltov, Y.: Formation of vertical fractures by means of highly viscous liquid. Proc Fourth World Pet Congr Rome. 579–586 (1955)
5. Geertsma, J., De Klerk, F.: Rapid method of predicting width and extent of hydraulically induced fractures. J. Pet. Technol. **21**, 1571–1581 (1969). https://doi.org/10.2118/2458-pa
6. Perkins, T.K., Kern, L.R.: Widths of hydraulic fractures. J. Pet. Technol. **13**, 937–949 (1961). https://doi.org/10.2118/89-pa
7. Nordgren, R.P.: Propagation of a vertical hydraulic fracture. Soc. Pet. Eng. J. **12**, 306–314 (1972). https://doi.org/10.2118/3009-pa
8. Settari, A.: Simulation of hydraulic fracturing processes. Soc. Pet. Eng. J. **20**, 487–500 (1980). https://doi.org/10.2118/7693-PA
9. Adachi, J., Siebrits, E., Peirce, A., Desroches, J.: Computer simulation of hydraulic fractures. Int. J. Rock Mech. Min. Sci. **44**, 739–757 (2007). https://doi.org/10.1016/j.ijrmms.2006.11.006
10. Yamamoto K, Shimamoto T, Maezumi S. Development of a true 3D hydraulic fracturing simulator. Soc Pet Eng - SPE Asia Pacific Oil Gas Conf Exhib 1999, APOGCE 1999 1999. https://doi.org/10.2523/54265-ms.
11. Yamamoto, K., Shimamoto, T., Sukemura, S.: Multiple fracture propagation model for a three-dimensional hydraulic fracturing simulator. Int J Geomech. **4**, 46–57 (2004). https://doi.org/10.1061/(ASCE)1532-3641(2004)4:1(46)

12. Boone, T.J., Ingraffea, A.R.: A numerical procedure for simulation of hydraulically-driven fracture propagation in POROELASTIC media. Int. J. Numer. Anal. Methods Geomech. **14**, 27–47 (1990)
13. Desroches, J., Thiercelin, M.: Modelling the propagation and closure of Micro-hydraulic fractures. Int. J. Rock Mech. Min. Sci. **30**, 1231–1234 (1993)
14. Pak A. Numerical modeling of hydraulic fracturing. PhD Thesis, Univ Alberta, Canada 1997
15. Simoni, L., Secchi, S.: Cohesive fracture mechanics for a multi-phase porous medium. Eng. Comput. **20**, 678–698 (2003)
16. Secchi, S., Simoni, L., Schrefler, B.A.: Mesh adaptation and transfer schemes for discrete fracture propagation in porous materials. Int. J. Numer. Anal. Methods Geomech. **31**, 331–345 (2007). https://doi.org/10.1002/nag
17. Réthoré, J., De Borst, R., Abellan, M.A.: A two-scale model for fluid flow in an unsaturated porous medium with cohesive cracks. Comput. Mech. **42**, 227–238 (2007). https://doi.org/10.1007/s00466-007-0178-6
18. Réthoré, J., De Borst, R., Abellan, M.A.: A two-scale approach for fluid flow in fractured porous media. Int. J. Numer. Methods Eng. **71**, 780–800 (2007). https://doi.org/10.1002/nme
19. Lobão, M.C., Eve, R., Owen, D.R., Souza Neto, E.A.: Modelling of hydro-fracture flow in porous media. Eng. Comput. **27**, 129–154 (2010). https://doi.org/10.1108/02644401011008568
20. Khoei, A.R., Barani, O.R., Mofid, M.: Modeling of dynamic cohesive fracture propagation in porous saturated media. Int. J. Numer. Anal. Methods Geomech. **35**, 1160–1184 (2011). https://doi.org/10.1002/nag
21. Barani OR, Khoei AR, Mofid M. Modeling of cohesive crack growth in partially saturated porous media ; a study on the permeability of cohesive fracture. Int. J. Fract. 2011;167:15–31. https://doi.org/10.1007/s10704-010-9513-6
22. Mohammadnejad, T., Khoei, A.R.: An extended finite element method for fluid flow in partially saturated porous media with weak discontinuities; the convergence analysis of local enrichment strategies. Comput. Mech. **51**, 327–345 (2012). https://doi.org/10.1007/s00466-012-0732-8
23. Mohammadnejad, T.: Khoei a. R. an extended finite element method for hydraulic fracture propagation in deformable porous media with the cohesive crack model. Finite Elem. Anal. Des. **73**, 77–95 (2013). https://doi.org/10.1016/j.finel.2013.05.005
24. Salimzadeh, S., Khalili, N.: A three-phase XFEM model for hydraulic fracturing with cohesive crack propagation. Comput. Geotech. **69**, 82–92 (2015). https://doi.org/10.1016/j.compgeo.2015.05.001
25. Khoei, A.R., Hirmand, M., Vahab, M., Bazargan, M.: An enriched FEM technique for modeling hydraulically driven cohesive fracture propagation in impermeable media with frictional natural faults : numerical and experimental investigations. Int. J. Numer. Methods Eng. **104**, 439–468 (2015). https://doi.org/10.1002/nme
26. Khoei, A.R., Vahab, M., Hirmand, M.: Modeling the interaction between fluid-driven fracture and natural fault using an enriched-FEM technique. Int. J. Fract. **197**, 1–24 (2015). https://doi.org/10.1007/s10704-015-0051-0
27. Vahab, M., Akhondzadeh, S., Khoei, A.R., Khalili, N.: An X-FEM investigation of hydro-fracture evolution in naturally-layered domains. Eng. Fract. Mech. **191**, 187–204 (2018). https://doi.org/10.1016/j.engfracmech.2018.01.025
28. Vahab M, Khalili N. Computational Algorithm for the Anticipation of the Fluid-Lag Zone in Hydraulic Fracturing Treatments 2018;18:1–15. https://doi.org/10.1061/(ASCE)GM.1943-5622.0001273
29. Vahab, M., Khalili, N.: A super-convergent staggered algorithm for the simulation of hydraulic fracturing treatments. Int. J. Fract. **217**, 1–16 (2019). https://doi.org/10.1007/s10704-019-00362-0
30. Mortazavi MS, Pirmoradi P, Khoei AR. Numerical simulation of cold and hot water injection into naturally fractured porous media using the extended – FEM and an equivalent continuum model 2022:0–39. https://doi.org/10.1002/nag.3314
31. Shi X, Qin Y, Xu H, Feng Q, Wang S, Xu P. Numerical simulation of hydraulic fracture propagation in conglomerate reservoirs 2021. https://doi.org/10.1016/j.engfracmech.2021.107738
32. Cong, Z., Li, Y., Tang, J., Martyushev, D.A.: Numerical simulation of hydraulic fracture height layer-through propagation based on three-dimensional lattice method. Eng. Fract. Mech. **264**, 108331 (2022). https://doi.org/10.1016/j.engfracmech.2022.108331
33. Rabczuk, T., Zi, G.: A Meshfree method based on the local partition of Unity for cohesive cracks. Comput. Mech. **39**, 743–760 (2006). https://doi.org/10.1007/s00466-006-0067-4
34. Khoshghalb, A., Khalili, N.: A meshfree method for fully coupled analysis of flow and deformation in unsaturated porous media. Int. J. Numer. Anal. Methods Geomech. **37**, 716–743 (2012). https://doi.org/10.1002/nag
35. Iranmanesh, M.A., Pak, A., Samimi, S.: Non-isothermal simulation of the behavior of unsaturated soils using a novel EFG-based three dimensional model. Comput. Geotech. **99**, 93–103 (2018). https://doi.org/10.1016/j.compgeo.2018.02.024
36. Liu, G.R.: Meshfree methods: moving beyond the finite element method. Boca Raton: CRC Press. (2003). https://doi.org/10.1115/1.1553432
37. Liu, G.R., Gu, Y.T.: An Introduction to Meshfree Methods and their Programming. Springer, Dordrecht, The Netherlands (2005). https://doi.org/10.1007/1-4020-3468-7
38. Modaressi, H., Aubert, P.: Element-free Galerkin method for deforming multiphase porous media. Int. J. Numer. Methods Eng. **340**, 313–340 (1998)
39. Oliaei, M.N., Soga, K., Pak, A.: Some numerical issues using element-free Galerkin mesh-less method for coupled hydro-mechanical problems. Int. J. Numer. Anal. Methods Geomech. **33**, 915–938 (2009). https://doi.org/10.1002/nag.747
40. Khoshghalb, A., Khalili, N.: A stable meshfree method for fully coupled flow-deformation analysis of saturated porous media. Comput. Geotech. **37**, 789–795 (2010). https://doi.org/10.1016/j.compgeo.2010.06.005
41. Soares Jr., D.: Iterative dynamic analysis of linear and nonlinear fully saturated porous media considering edge-based smoothed meshfree techniques. Comput. Methods Appl. Mech. Eng. **253**, 73–88 (2013). https://doi.org/10.1016/j.cma.2012.10.010
42. Tootoonchi, A., Khoshghalb, A., Liu, G.R., Khalili, N.: A cell-based smoothed point interpolation method for flow-deformation analysis of saturated porous media. Comput. Geotech. **75**, 159–173 (2016). https://doi.org/10.1016/j.compgeo.2016.01.027
43. Ghaffaripour, O., Khoshghalb, A., Khalili, N.: An edge-based smoothed point interpolation method for elasto-plastic coupled hydro-mechanical analysis of saturated porous media. Comput. Geotech. **82**, 99–109 (2017). https://doi.org/10.1016/j.compgeo.2016.10.002
44. Samimi, S., Pak, A.: Three-dimensional simulation of fully coupled hydro-mechanical behavior of saturated porous media using element free Galerkin (EFG) method. Comput. Geotech. **46**, 75–83 (2012). https://doi.org/10.1016/j.compgeo.2012.06.004
45. Samimi, S., Pak, A.: A novel three-dimensional element free Galerkin (EFG) code for simulating two-phase fluid flow in porous materials. Eng Anal Bound Elem. **39**, 53–63 (2014). https://doi.org/10.1016/j.enganabound.2013.10.011
46. Samimi, S., Pak, A.: A three-dimensional mesh-free model for analyzing multi-phase flow in deforming porous media. Meccanica. **51**, 517–536 (2015). https://doi.org/10.1007/s11012-015-0231-z
47. Belytschko, T., Krongauz, Y., Fleming, M., Organ, D., Snm Liu, W.K.: Smoothing and accelerated computations in the element free Galerkin method. J. Comput. Appl. Math. **74**, 111–126 (1996). https://doi.org/10.1016/0377-0427(96)00020-9

48. Organ, D., Fleming, M., Terry, T., Belytschko, T.: Continuous meshless approximations for nonconvex bodies by diffraction and transparency. Comput. Mech. **18**, 225–235 (1996). https://doi.org/10.1007/BF00369940
49. Fleming, M., Chuu, Y.A., Moran, B., Belytschko, T.: Enriched element-free Galerkin methods for crack tip fields. Int. J. Numer. Methods Eng. **40**, 1483–1504 (1997). https://doi.org/10.1002/(SICI)1097-0207(19970430)40:8<1483::AID-NME123>3.0.CO;2-6
50. Ventura, G., Xu, J.X., Belytschko, T.: A vector level set method and new discontinuity approximations for crack growth by EFG. Int. J. Numer. Methods Eng. **54**, 923–944 (2002). https://doi.org/10.1002/nme.471
51. Rabczuk, T., Belytschko, T.: Cracking particles: a simplified meshfree method for arbitrary evolving cracks. Int. J. Numer. Methods Eng. **61**, 2316–2343 (2004). https://doi.org/10.1002/nme.1151
52. Cordes, L.W.W., Moran, B.: Treatment of material discontinuity in the element-free Galerkin method. Comput. Methods Appl. Mech. Eng. **139**, 75–89 (1996). https://doi.org/10.1016/S0045-7825(96)01080-8
53. Nguyen, V.P., Rabczuk, T., Bordas, S., Duflot, M.: Meshless methods: a review and computer implementation aspects. Math. Comput. Simul. **79**, 763–813 (2008). https://doi.org/10.1016/j.matcom.2008.01.003
54. Iranmanesh, M.A., Pak, A.: Extrinsically enriched element free Galerkin method for heat and fluid flow in deformable porous media involving weak and strong discontinuities. Comput. Geotech. **103**, 179–192 (2018). https://doi.org/10.1016/j.compgeo.2018.07.013
55. Oliaei, M., Pak, A., Soga, K.: A coupled hydro-mechanical analysis for prediction of hydraulic fracture propagation in saturated porous media using EFG mesh-less method. Comput. Geotech. **55**, 254–266 (2014)
56. Samimi, S., Pak, A.: A fully coupled element-free Galerkin model for hydro-mechanical analysis of advancement of fluid-driven fractures in porous media. Int. J. Numer. Anal. Methods Geomech. **40**, 2178–2206 (2016). https://doi.org/10.1002/nag
57. Biot, M.A.: General theory of three-dimensional consolidation. J. Appl. Phys. **12**, 155–164 (1941). https://doi.org/10.1063/1.1712886
58. Khoei, A.R.: Extended finite element method. Wiley. (2014). https://doi.org/10.1016/C2012-0-01326-9
59. Lewis, R.W., Schrefler, B.A.: The finite element method in the static and dynamic deformation and consolidation of porous media. Chichester: Wiley. (1998). https://doi.org/10.1137/1031039
60. Witherspoon, P.A., Wang, J.S.Y., Iwai, K., Gale, J.E.: Validity of cubic law for fluid flow in a deformable rock fracture. Water Resour. Res. **16**, 1016–1024 (1980)
61. Schrefler, B.A., Zhan, X., Simoni, L.: A coupled model for water flow, airflow and heat flow in deformable porous media. Int J Numer Methods Heat Fluid Flow. **5**, 531–547 (1995)
62. Zi, G., Rabczuk, T., Wall, W.: Extended meshfree methods without branch enrichment for cohesive cracks. Comput. Mech. **40**, 367–382 (2007). https://doi.org/10.1007/s00466-006-0115-0
63. Moës, N., Cloirec, M., Cartraud, P., Remacle, J.F.: A computational approach to handle complex microstructure geometries. Comput. Methods Appl. Mech. Eng. **192**, 3163–3177 (2003). https://doi.org/10.1016/S0045-7825(03)00346-3
64. Barenblatt, G.I.: The formation of equilibrium cracks during brittle fracture . general ideas and hypotheses. Axially-symmetric cracks. J. Appl. Math. Mech. **23**, 622–636 (1959)
65. Sarris, E., Papanastasiou, P.: The influence of the cohesive process zone in hydraulic fracturing modelling. Int. J. Fract. **167**, 33–45 (2011). https://doi.org/10.1007/s10704-010-9515-4